ADVANCES IN PHYSICS: X, 2016
VOL. 1, NO. 4, 640–660
http://dx.doi.org/10.1080/23746149.2016.1232177

Taylor & Francis
Taylor & Francis Group

REVIEW ARTICLE

OPEN ACCESS

Recent advances in identifying the structure of liquid and glassy oxide and chalcogenide materials under extreme conditions: a joint approach using diffraction and atomistic simulation

Shinji Kohara[a,b,c,d] and Philip S. Salmon[e]

[a]Synchrotron X-ray Group, Light/Quantum Beam Field, Research Center for Advanced Measurement and Characterization, National Institute for Materials Science (NIMS), Sayo-cho, Japan; [b]Modeling Group, Information Integrated Explorative Research Field, Center for Materials Research by Information Integration, NIMS, Tsukuba, Japan; [c]Research & Utilization Division, Japan Synchrotron Radiation Research Institute, Sayo-cho, Japan; [d]PREST, Japan Science and Technology Agency, Tokyo, Japan; [e]Department of Physics, University of Bath, Bath, UK

ABSTRACT

The advent of advanced instrumentation and measurement protocols makes it increasingly feasible to use X-ray and neutron diffraction methods to investigate the structure of liquid and glassy materials under extreme conditions of high-temperatures and/or high-pressures. In particular, a combination of diffraction and modern simulation techniques is allowing for an understanding of the structure of these disordered materials at both the atomistic and electronic levels. In this article, we highlight some of the recent work in solving the structure of liquid and glassy oxide and chalcogenide materials under extreme conditions. We consider, in turn, the use of aerodynamic levitation with laser heating to investigate the structure of high-temperature oxide melts and to fabricate novel glassy materials by container-less processing; the use of high-pressure methods in the gigapascal regime to investigate the mechanisms of network collapse for glassy network structures; and the simultaneous application of high-pressures and high-temperatures to explore the structure of disordered materials. Finally, we consider the use of other quantum-beam diffraction-based techniques for probing the order hidden in the correlation functions that describe the structure of disordered matter.

ARTICLE HISTORY
Received 13 January 2016
Accepted 31 August 2016

KEYWORDS
Structure; liquids; glasses; X-ray diffraction; neutron diffraction; high temperatures; high pressures; atomistic simulations

PACS
61.05.cp: X-ray diffraction;
61.05.fm: Neutron diffraction;
61.20.-p: Structure of liquids;
61.43.Fs: Glasses

CONTACT Shinji Kohara KOHARA.Shinji@nims.go.jp

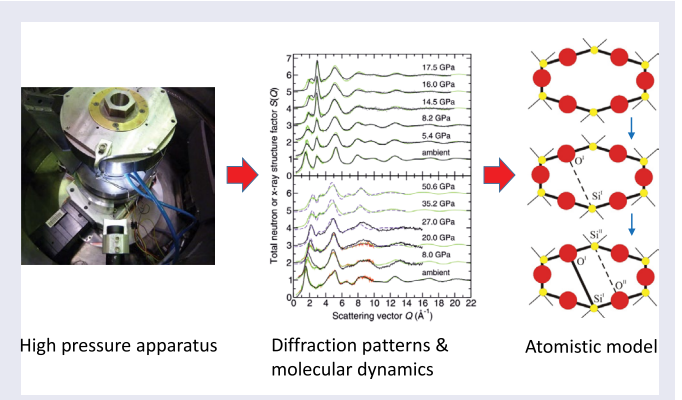

1. Introduction

The absence of translational periodicity and the complexity associated with the structure of liquid and glassy materials makes for a challenging field of research. Indeed, as noted by Egelstaff in his review article of 1983 [1], solving the structure of these materials can make for a frustrating time: Although the underlying concepts have been known for a long while, the capability for making high-quality diffraction experiments, especially under different state conditions, is often unavailable. However, the advent of advanced X-ray and neutron diffraction instrumentation and measurement protocols, when combined with modern computational methods [2], makes it increasingly possible to understand the structure of liquids and glasses at both the atomistic and electronic levels. In particular, it is possible to go beyond the nearest-neighbour information on inter-atomic distances and mean coordination numbers that is provided by the total structure factor measured in a single X-ray or neutron diffraction experiment [3,4]. Here, the relationship between experiment and simulation is symbiotic: experiment is required to test the efficacy of the theoretical scheme used in a simulation but, once this scheme has been established, the models can be used to enhance the information made available. Ideally these models will also have predictive capabilities, e.g. for new compositions and/or state conditions.

In this article, we focus on the structure of oxide and chalcogenide liquids and glasses under extreme conditions of high temperatures and/or high pressures. In particular, we use case-examples taken from the recent literature in order to illustrate recent advances in diffraction techniques, and the type of information that can now be obtained using a joint diffraction and simulation approach. The results from other experimental techniques are referred to when appropriate. The paper is organised as follows. In Section 2, the essential theory for diffraction experiments is summarised. In Section 3, the structure of aerodynamically levitated oxide liquids is considered, along with the structure of the glasses that can be obtained from levitated liquids. In Section 4, the structure of oxide and

chalcogenide glasses at high pressures is discussed. In Section 5, an account is given of the diffraction methods used to investigate liquids at high pressure and high temperature conditions. For disordered oxide materials, the oxygen packing fraction is found to play a key role in determining when network transformations are likely to occur. Finally, in Section 6 we consider future directions for probing the order hidden in the correlation functions that describe the structure of disordered matter.

2. Outline diffraction theory

In an X-ray or neutron diffraction experiment on a disordered material containing n chemical species, information on the structure is contained in the total structure factor [4,5]

$$S(Q) = 1 + \frac{1}{|\langle w(Q)\rangle|^2} \sum_{\alpha=1}^{n} \sum_{\beta=1}^{n} c_\alpha c_\beta w_\alpha^*(Q)\, w_\beta(Q) \left[S_{\alpha\beta}(Q) - 1\right] \tag{1}$$

where c_α is the atomic fraction of chemical species α; $w_\alpha(Q)$ is either a Q-dependent atomic form factor with dispersion terms in X-ray diffraction (XRD) or a Q-independent coherent scattering length in neutron diffraction and is, in general, a complex number; $S_{\alpha\beta}(Q)$ is a partial structure factor; and $|\langle w(Q)\rangle|^2 = \sum_{\alpha=1}^{n} \sum_{\beta=1}^{n} c_\alpha c_\beta w_\alpha^*(Q)\, w_\beta(Q)$. A subscript/superscript X or N can be used to distinguish between the $S(Q)$ functions measured by X-ray and neutron diffraction, respectively. The corresponding real-space information is contained in the total pair-distribution function $G(r)$, which is obtained from the Fourier transform relation

$$G(r) = 1 + \frac{1}{2\pi^2 \rho r} \int_0^\infty Q[S(Q) - 1] \sin(Qr) \mathrm{d}Q \tag{2}$$

where r is a distance in real-space and ρ is the atomic number density. A similar Fourier transform relation can be used to convert a partial structure factor $S_{\alpha\beta}(Q)$ into a partial pair-distribution function $g_{\alpha\beta}(r)$. The structure of a system containing n chemical species is described by $n(n+1)/2$ of these partial pair-correlation functions.

3. Levitated oxide liquids and the glasses obtained from levitated liquids

Levitation methods [6] allow for an investigation of high-temperature liquids without the difficulties, such as contamination, associated with a container. These container-less methods also permit the formation of deeply undercooled liquids, via the elimination of extrinsic heterogeneous nucleation centres, and thus enable

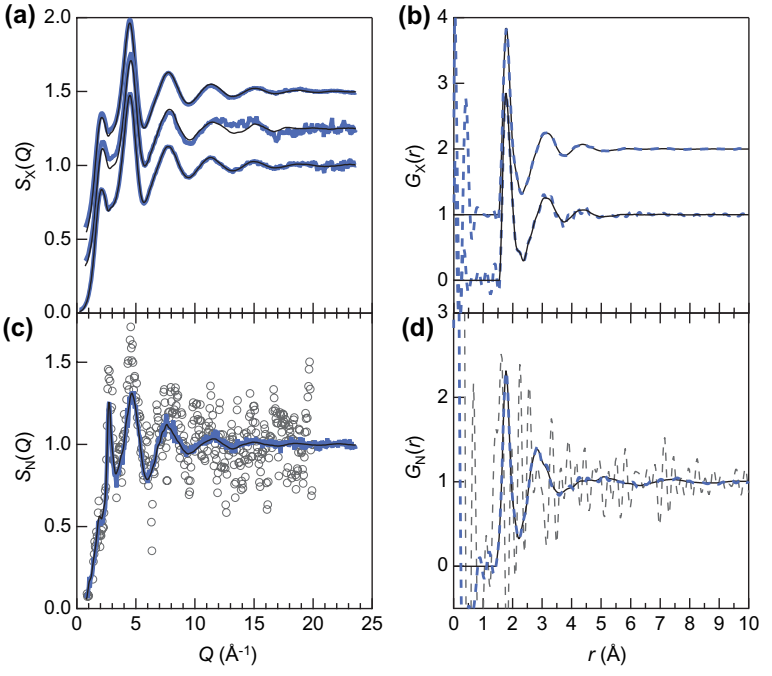

Figure 1. The measured (a) X-ray and (c) neutron total structure factors $S(Q)$, and (b) X-ray and (d) neutron total pair-distribution functions $G(r)$ for l-Al_2O_3 at 2400 K [7]. The solid circles in (a) correspond to the measurements made at three different synchrotron sources, and the curves in (b) are the Fourier transforms of two of these data-sets with the unphysical oscillations at $r < 1.5$ Å set to the $G(r \rightarrow 0)$ limit. The open and solid circles in (c) correspond to old [13] and modern [7] measurements, respectively, and the broken and solid curves in (d) are the Fourier transforms of these data-sets, respectively. In (d), the unphysical oscillations at $r < 1.5$ Å for the latest $G(r)$ function are set to the $G(r \rightarrow 0)$ limit. The solid curves that are superposed on the solid circles in (a) and (c) give the back Fourier transforms of the corresponding $G(r)$ functions after the unphysical oscillations at $r < 1.5$ Å are set to the $G(r \rightarrow 0)$ limit.

the fabrication of novel glassy materials. Accordingly, there has been much work on the atomic structure of levitated oxide liquids [6–10], and on the glasses synthesised from levitated liquids [6,10,11], using X-ray and neutron diffraction. Of the different levitation techniques that can be used [6], aerodynamic levitation with laser heating is the most popular because the instrumentation is compact and works well for a wide variety of materials. We will focus on recent work to uncover the structure of the high-temperature oxide liquids Al_2O_3 [7], ZrO_2 [8] and UO_2 [9] as well as the structure of materials in the fragile glass-forming system CaO–Al_2O_3 in their high-temperature liquid and/or glassy forms [10–12]. Previous work on oxide liquids is reviewed elsewhere [6].

3.1. Structure of liquid Al_2O_3

Liquid (l-) Al_2O_3 is a much studied melt, partly because it is well known as a non-glass-forming liquid. Figure 1 shows the X-ray and neutron total structure

factors $S(Q)$ and pair-distribution functions $G(r)$ for l-Al_2O_3 near to its melting point [7,13]. As indicated by Figure 1(a) and (b), the XRD data-sets measured at different synchrotron sources are self-consistent and, as indicated by Figure 1(c) and (d), neutron diffraction can now deliver high-quality structural information on aerodynamically levitated materials. In general, there is a contrast between the weighting factors $w_\alpha(Q)$ in Equation (1) for X-ray and neutron diffraction. These methods will therefore deliver complementary information on the structure of a liquid, as indicated by the notable contrast between the X-ray and neutron $S(Q)$ functions in the low-Q region of Figure 1(a) and (c). In Ref. [7], a molecular dynamics model that gave best agreement with experiment was refined using the reverse Monte Carlo (RMC) method. The melt structure was found to be composed predominantly of AlO_4 and AlO_5 polyhedra, in the approximate ratio of 2:1, where the majority of these polyhedra are corner-sharing. Edge-sharing conformations do, however, have a notable presence at the ~16% level, and most of the oxygen atoms (~81%) are shared among three or more polyhedra. This model for the liquid, in which AlO_4 tetrahedra are the predominant structural motifs, is consistent with the information available from high-temperature ^{27}Al nuclear magnetic resonance (NMR) experiments [14]. A comparison with Zachariasen's rules helps to explain why liquid Al_2O_3 is not a glass-forming material. Glass-forming tendency would be favoured if the Al and O atoms were fourfold and twofold coordinated, respectively, and if edge-sharing conformations were rare [7].

3.2. Topological ordering and glass-forming ability

Figure 2(a) compares the Bhatia–Thornton number–number partial structure factor $S_{NN}(Q)$ for the high-temperature liquid phases of Al_2O_3, ZrO_2 and SiO_2 as obtained from molecular dynamics simulations that reproduce the measured total structure factors [8]. For these A_2X_3 and AX_2 materials, $S_{NN}(Q) \equiv c_A^2 S_{AA}(Q) + c_X^2 S_{XX}(Q) + 2c_A c_X S_{AX}(Q)$ describes the topological ordering [15]. Only l-SiO_2 forms a glass, and its structure exhibits pronounced intermediate range ordering as manifested by the appearance of a prominent first-sharp diffraction peak (FSDP) in $S_{NN}(Q)$ at $Q\,r_{AX} = 2.7$. The SiO_2 glass structure is formed from SiO_4 tetrahedra that self-assemble as the liquid is cooled to give a broad distribution of ring sizes that incorporate between 3 and 12 Si atoms, where these rings form the boundaries of topologically disordered cages [8]. The ring size distribution obtained from the RMC model is broader than that from the molecular dynamics simulation. In comparison, only sixfold rings, incorporating six Si atoms, contribute to the structure of the β-cristobalite phase of crystalline c-SiO_2 (Figure 2(b)). The position Q_{FSDP} of the FSDP arises from an underlying real-space periodicity $2\pi/Q_{FSDP}$ that originates, e.g. from the formation of pseudo Bragg planes in l-SiO_2, as indicated by the broken curves in Figure 2(b). The appearance of transient-layered structures in glass-forming melts is discussed elsewhere [16]. The absence of translational periodicity in the glass and its associated liquid,

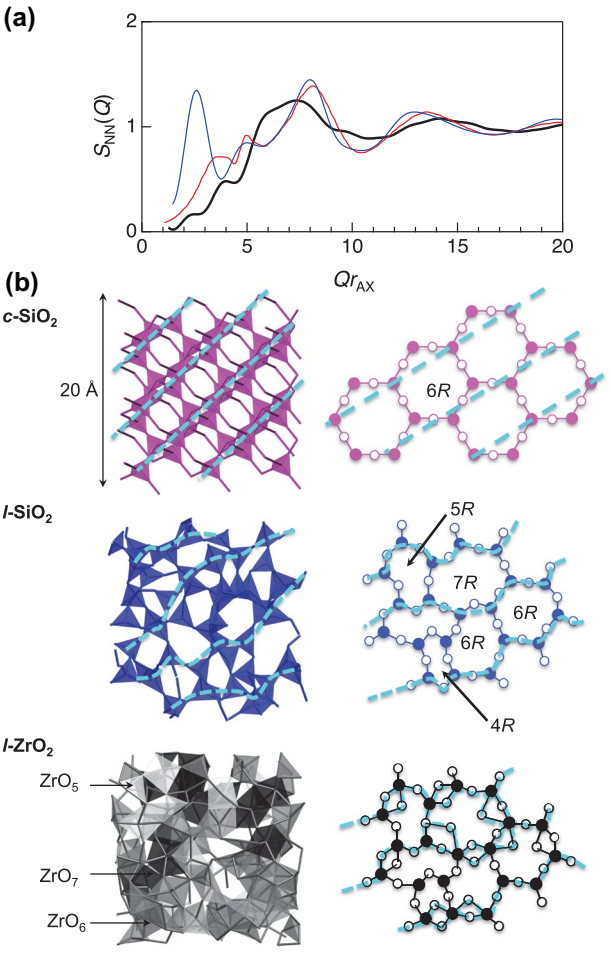

Figure 2. The (a) Bhatia–Thornton number–number partial structure factor $S_{NN}(Q)$ for *l*-Al_2O_3 at 2400 K (solid light (red) curve), *l*-ZrO_2 at 3073 K (solid bold (black) curve) and *l*-SiO_2 at 2373 K (solid dark (blue) curve) derived from molecular dynamics simulations [8]. The scattering vector Q is scaled by the nearest-neighbour distance r_{AX} for unlike chemical species. (b) Polyhedral representations and schematic illustrations of the atomic configurations in *c*-SiO_2, *l*-SiO_2 and *l*-ZrO_2. The underlying periodicity of a structure is indicated by the broken (cyan) curves [8]. For *c*-SiO_2 and *l*-SiO_2, the number of Si atoms in a ring is also indicated, e.g. 6*R* refers to a ring with 6 Si atoms.

and the presence of topological disorder, manifest themselves in the finite width ΔQ_{FSDP} of the FSDP, i.e. there is a finite correlation length of $2\pi/\Delta Q_{FSDP}$ associated with the intermediate range ordering [17].

As for the case of *l*-Al_2O_3, a pronounced FSDP does not appear in $S_{NN}(Q)$ for *l*-ZrO_2 (Figure 2(a)), i.e. both structures are less regular than for *l*-SiO_2 (Figure 2(b)) and there is an absence of intermediate range ordering on a real-space length scale of $2\pi/Q_{FSDP}$. In the case of *l*-ZrO_2, this situation arises from the formation of a variety of Zr-centred structural motifs with large oxygen coordination numbers,

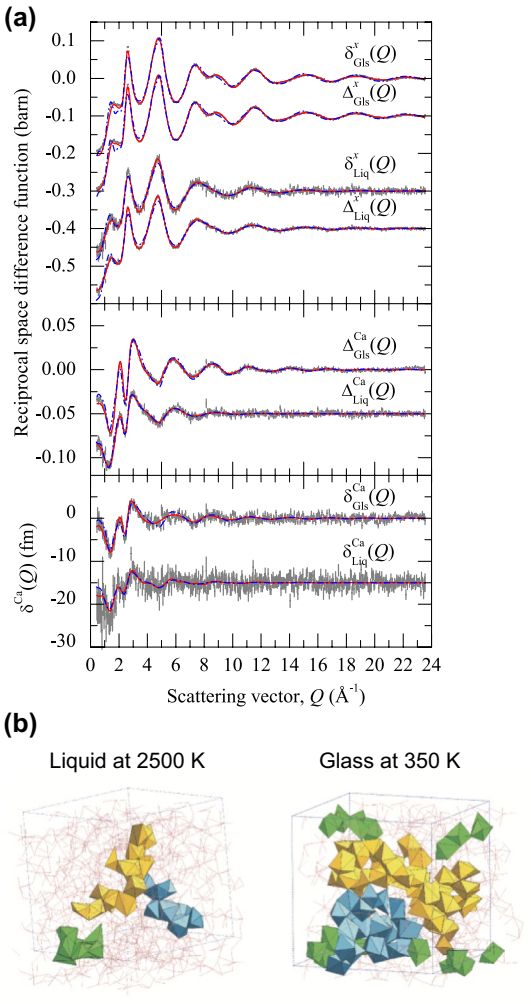

Figure 3. (a) The difference functions $\Delta^{x}(Q)$, $\delta^{x}(Q)$, $\Delta^{Ca}(Q)$ and $\delta^{Ca}(Q)$ for glassy (Gls) and liquid (Liq) $CaAl_2O_4$. The vertical bars show the statistical errors on the measured data points, and the solid (red) curves show the back Fourier transforms of the corresponding real-space functions. The chained (blue) curves show molecular dynamics results [10]. (b) Snapshots illustrating the largest clusters of edge-sharing Ca-centred polyhedra in the molecular dynamics simulations of $CaAl_2O_4$ for the liquid at 2500 K (left) and for the glass at 350 K (right) [10].

predominantly ZrO_5, ZrO_6 and ZrO_7, many of which are edge-sharing. For network glass-forming materials with the AX_2 stoichiometry, a diminished FSDP is a signature of increased melt fragility, i.e. with an increase in the rate of change in viscosity with temperature as the glass transition is approached [18]. The absence of an FSDP in $S_{NN}(Q)$ for single-component oxide materials such as *l*-Al_2O_3 and *l*-ZrO_2 may therefore be an important indicator of non-glass-forming tendency, reflecting the existence of low-viscosity liquids [8].

3.3. Structure of liquid and glassy calcium aluminates

The method of neutron diffraction with isotope substitution is a powerful element-specific structural probe [4]. Recently, this method was applied with Ca isotopes to a laser-heated levitated-liquid of $CaAl_2O_4$ at 1973 K, and to the corresponding glass at 300 K [10]. Figure 3(a) shows the measured difference functions $\Delta^{Ca}(Q)$, $\delta^{Ca}(Q)$, $\Delta^{x}(Q)$, and $\delta^{x}(Q)$ for glassy and liquid $CaAl_2O_4$, which are in good agreement with those obtained from molecular dynamics simulations made using an ionic interaction model that accounts for anion polarisation and shape deformation effects, as well as the polarisability of the calcium cations. Here, $\Delta^{Ca}(Q)$ has contributions from only the Ca–Ca and Ca-μ pair-correlation functions where μ denotes Al or O, whereas $\delta^{Ca}(Q)$ involves only the Ca-μ pair-correlation functions. In contrast, $\Delta^{x}(Q)$ involves both the Ca–Ca and μ-μ pair-correlation functions, whereas $\delta^{x}(Q)$ involves only the μ-μ pair-correlation functions.

The results show that significant structural changes occur on vitrification of this fragile glass-forming material on both the local and intermediate length scales [10]. Firstly, there is a reorganisation on quenching that leads to a reduction in the Al–O coordination number from 4.20(4) to 4.04(3), corresponding to a removal of the AlO_5 polyhedra and threefold-coordinated oxygen atoms that are present in the liquid, and the establishment of a network of corner-sharing AlO_4 tetrahedra in the glass. The liquid state coordination number of 4.20(4) compares to an estimate of 4.16 from high-temperature ^{27}Al NMR experiments, based on the temperature dependence of the chemical shift [19]. Secondly, edge-sharing Ca-centred polyhedra occur in the liquid, and there is an enhancement of these connections in the glass (Figure 3(b)). This observation is consistent with another joint experimental and simulation study that involved X-ray and neutron diffraction along with extended X-ray absorption fine structure (EXAFS) spectroscopy, and a modelling procedure in which the atomistic configurations generated using RMC were used as the starting point for density functional theory (DFT) based simulations [11]. Figure 4(a)–(c) compare the measured neutron and X-ray total structure factors $S(Q)$ and the EXAFS $k^3\chi(k)$ function (measured at the Ca K-edge) for glassy 50CaO-50Al_2O_3 (50CaO) and glassy 64CaO-36 Al_2O_3 (64CaO) with the results obtained from the DFT–RMC models [11]. There is little change in the diffraction or EXAFS data-sets as the composition is varied, which indicates similar glass structures.

The electride glass $[Ca_{24}Al_{28}O_{64}]^{4+}\cdot 4e^-$ (C12A7:e^-), which is synthesised from a strongly reduced high-temperature melt, contains trapped electrons that are solvated by cations in the glass structure, an unusual feature for an oxide material [12]. It has been assumed that these solvated electrons are trapped in the cage structures that are formed when excess oxygen atoms in the C12A7 melt are removed from AlO_5 or AlO_6 units. To explore this possibility [11], one oxygen atom was removed from the modelled 64CaO glass structure to leave a cavity marked as h_2 in Figure 4(d), while two additional electrons were introduced in

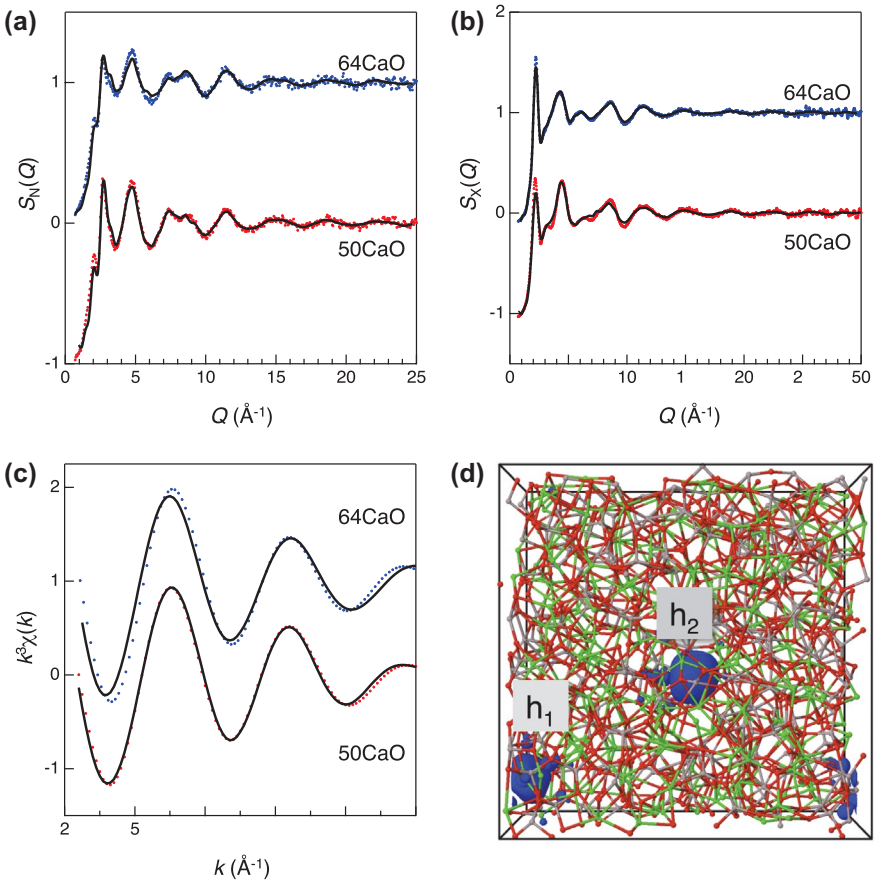

Figure 4. The (a) neutron and (b) X-ray total structure factors $S(Q)$ and (c) EXAFS $k^3\chi(k)$ data for glassy 50CaO and 64CaO. The EXAFS $k^3\chi(k)$ data, where k denotes the photoelectron wave vector [3], were obtained by back Fourier transforming the first correlation peak in |FT|. The experimental data points are given by coloured circles, and the results from DFT–RMC models are given by dark (black) curves [11]. In (d), a ball-and-stick representation is given for the atomic configurations in an electride glass, where one oxygen atom (located at h_2) was removed from the DFT–RMC model for 64CaO glass and two electrons were added. The electron spin density for these electrons is shown for the case when they have the same spin (blue regions). One electron is located in the cavity at h_2 and the other is located in a cavity at h_1, where the cavity separation is 12 Å [11].

order to maintain overall charge neutrality. DFT-based simulations were then used to optimise the structure for different spin configurations of these electrons. In the spin-degenerate case, where there is no distinction concerning the 'spin' of the electrons, they both occupy the h_2 cavity, and yield the highest occupied molecular orbital that is similar to the lowest unoccupied molecular orbital of the unmodified 64CaO glass. However, removal of the spin-degeneracy (triplet-spin configuration) leads to an electronic configuration that is 0.97 eV more energetically favourable, where the two additional electrons have the same spin and are located in well-separated cavities that are labelled by h_1 and h_2 in Figure 4(d) (h_1

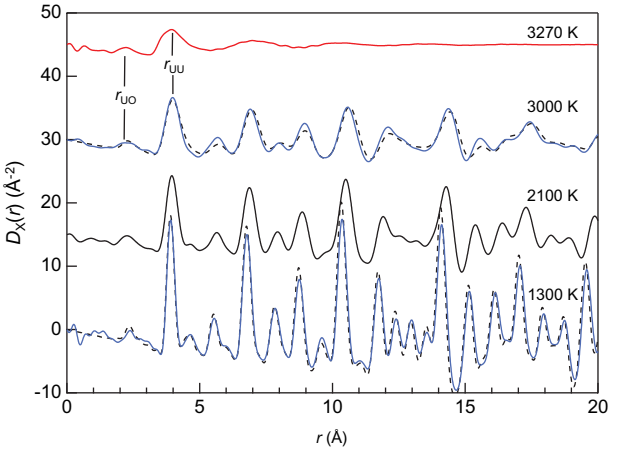

Figure 5. The temperature dependence of the X-ray pair-distribution function $D_X(r)$ for UO_2 in its crystalline (1300–3000 K) and liquid (3270 K) phases [9] as measured by diffraction (solid curves) or simulated using molecular dynamics (broken curves). The nearest neighbour U–O and U–U distances at the highest temperatures are indicated by r_{UO} and r_{UU}, respectively.

is a cavity in the host 64CaO glass structure). This procedure was repeated for two, three and four removed oxygen atoms, corresponding to four, six and eight additional electrons, respectively. In every case, separated (solvated) electrons in individual cavities were found to be more energetically favourable than two electrons in the same cavity (F-centre-like states). The removal of increasing numbers of oxygen atoms increases the number of defect states in the electronic band gap and thereby increases the electrical conductivity, thus giving the possibility of an electride glass with tuneable electrical properties [11].

3.4. Structure of UO_2 on melting

UO_2 is an important fuel in fission power reactors but there has been little experimental information on the structure of the liquid phase, which is relevant for reactor safety, because of the high-temperatures involved and the corrosion caused by the melt. Recently, it has proved possible, however, to tackle this problem using aerodynamic levitation with laser heating and XRD [9]. Figure 5 shows the temperature dependence of the X-ray pair-distribution function $D_X(r) \equiv 4\pi\rho r\left[G_X(r) - 1\right]$ for UO_2 in both its crystalline solid and liquid phases, covering a temperature range of 1300–3270 K. On melting, there is a marked drop in the average U–O coordination number from 8 to 6.7 ± 0.5 and molecular dynamics simulations, made with pair-potentials that were refined using the diffraction results, show a distribution of U-centred oxygen polyhedra. The simulations predict a liquid state mobility for the chemical species that is higher than found from a model of the liquid in which there is no change to the U–O coordination number on melting [9].

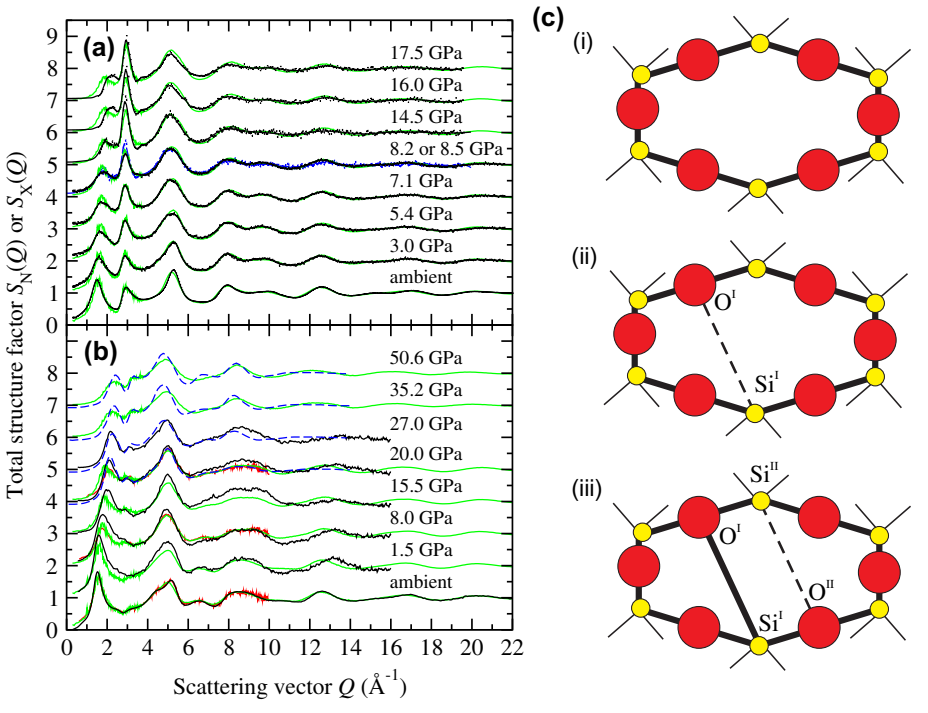

Figure 6. The pressure dependence of the (a) neutron and (b) X-ray total structure factors $S(Q)$ for SiO_2 glass under cold compression. The solid light (green) curves are from molecular dynamics simulations, and all other curves represent measured data sets [26]. (c) Schematic of a series of ring closure events in SiO_2 glass where the Si atoms are small (yellow) circles and the O atoms are large (red) circles. The initial primitive ring is shown in (i), a single ring closure event is shown in (ii) and a second ring closure event is shown in (iii). At a given stage in the densification process, existing Si–O bonds within a ring are shown by thick solid lines and the new Si–O bond is shown by a broken line. The remainder of the Si–O bonds are indicated by thin solid lines [26].

4. Oxide and chalcogenide glasses at high pressures

The response of liquid and glass structures to high-pressure conditions, and the mechanisms of network collapse, are of importance in fields that range from materials processing to geophysics. The measurement of accurate diffraction patterns is, however, challenging because of the need for small samples and the appearance of unwanted scattering from high-pressure apparatus. Diamond anvil cells have long been used with XRD to investigate the structure of disordered materials at pressures in the gigapascal (GPa) regime, where the background signal (primarily Compton scattering from diamond) can be reduced substantially using perforated diamond anvils [20]. More recently, the development of new instrumentation and measurement protocols has enabled accurate neutron diffraction patterns to be measured for glassy materials using a Paris–Edinburgh press [21], first at pressures up to 8.6 GPa [22], and then at pressures up to 17.5 GPa using a different scattering geometry [23]. Neutron diffraction with a multi-anvil press has also been applied to investigate the structure of SiO_2 glass at pressures up to 9.4 GPa [24].

The development of *in situ* high-pressure neutron diffraction to investigate the structure of glasses and liquids is reviewed elsewhere [25]. In order to illustrate the advances that have been made, we will focus on the structures of the prototypical glassy materials SiO_2 [26], B_2O_3 [27] and $GeSe_2$ [28] under cold compression, i.e. pressurisation at ambient temperature.

4.1. Structure of glassy SiO_2 under pressure

Figure 6(a) and (b) show the pressure dependence of the total structure factors measured for glassy SiO_2 by neutron diffraction and XRD, respectively [26,29–31]. These methods are more sensitive to the O and Si atom pair-correlation functions, respectively, and the complementarity of the information thus provided is indicated by the presence at ambient pressure of a so-called principal peak in $S_N(Q)$ at ~2.9 $Å^{-1}$ but an absence of this feature in $S_X(Q)$. The X-ray data-sets cover a pressure range over which there is a transformation of the glass structure from a network made from corner-sharing SiO_4 tetrahedra to a network made from edge- and corner-sharing SiO_6 octahedra. Both sets of diffraction patterns can be accounted for by molecular dynamics simulations using the Tangney-Scandolo [32] interaction potentials, which incorporate anion (dipole) polarisation terms (Figure 6(a) and (b)). The atomistic configurations thus provided show that densification proceeds via the formation of fivefold-coordinated Si atoms. Strikingly, the modelled rate of change with pressure of the mean primitive ring size (a ring is primitive if it cannot be decomposed into smaller rings) can be accounted for by a simple 'zipper' model for ring closure (Figure 6(c)) [26]. Here, a primitive ring closes when a silicon atom Si^I forms an additional bond with another oxygen atom O^I within the ring, thus increasing the Si^I coordination number from four to five and the O^I coordination number from two to three (Figure 6(c)(ii)). A further ring closure event then takes place at an adjacent site to give another over-coordinated silicon atom Si^{II} along with an additional threefold-coordinated oxygen atom O^{II} (Figure 6(c)(iii)). The proximity of these ring closure events helps to preserve locally the glass stoichiometry and, because the Si and O atoms in the Tangney-Scandolo interaction model are charged, this acts in a direction to preserve local charge neutrality.

4.2. Structure of glassy B_2O_3 under pressure

The pressure dependence of the total structure factors measured for glassy B_2O_3 by neutron diffraction and XRD are shown in Figure 7(a) and (b), respectively [27,33]. Here, the complementary nature of the information provided by these structural probes is indicated by the differences between the diffraction patterns at a given pressure, where neutron diffraction and XRD are more sensitive to the B and O atom pair-correlation functions, respectively. The diffraction results show pressure-induced changes in the B–O bond length (Figure 7(c)) and to the B–O

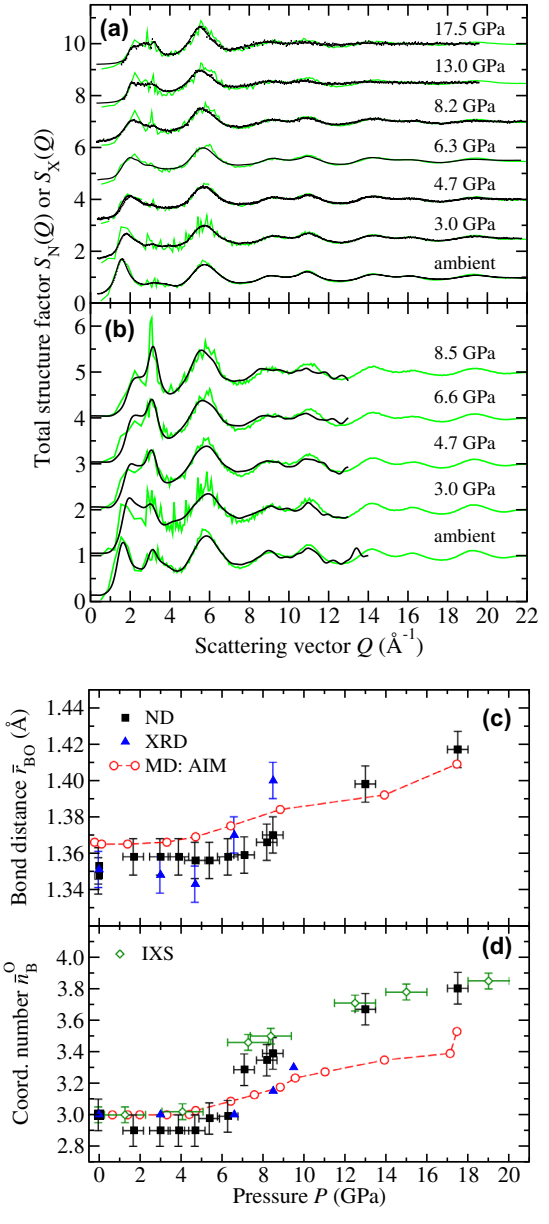

Figure 7. The pressure dependence of the (a) neutron and (b) X-ray total structure factors $S(Q)$ for B_2O_3 glass under cold compression. The dark solid (black) curves give the measured data-sets, and the solid light (green) curves are from molecular dynamics simulations using an aspherical ion model (AIM) [27]. The pressure dependence of the mean (c) B–O bond distance $\bar{r}_{BO}$ and (d) B–O coordination number $\bar{n}_B^O$, where the results obtained from neutron diffraction (ND) [27], X-ray diffraction (XRD) [33] and inelastic X-ray scattering (IXS) [34] experiments are compared to those obtained from molecular dynamics simulations using the AIM [27].

coordination number, where the latter increases from three to four (Figure 7(d)). The neutron diffraction results tie together the coordination numbers obtained from previous XRD [33] and inelastic X-ray scattering [34] experiments. In Figure

7(a)–(d), the experimental results are compared to those obtained from molecular dynamics simulations made using a newly developed aspherical ion model in which the size and shape of the oxide anions is allowed to change in response to their coordination environment [27]. The molecular dynamics results reproduce the main features in the measured neutron and X-ray $S(Q)$ functions, although there is discrepancy between the simulated and measured B–O bond distances and coordination numbers. Nevertheless, the overall results, when supplemented by those obtained from *in situ* high-pressure Raman spectroscopy experiments [35], reveal three densification regimes. At ambient pressure, the network structure of B_2O_3 is constructed from corner-sharing planar BO_3 triangular motifs, where the majority link to make super-structural units in the form of planar B_3O_9 boroxol rings. Initially, as the pressure is increased from ambient to ~6.3 GPa, these rings dissolve and there is an attendant change in the intermediate range ordering. As the pressure is further increased, BO_4 motifs replace BO_3 triangles and the dissolution of boroxol rings continues until it is completed by 11–14 GPa. Thereafter, the mean B–O coordination number continues to increase with pressure to give a predominantly tetrahedral glass, a process that is completed at a pressure in excess of 22.5 GPa.

4.3. Structure of glassy $GeSe_2$ under pressure

For $GeSe_2$ glass, conventional X-ray and neutron diffraction experiments yield almost identical information [4]. This situation arises from the similarity between the X-ray form factors for Ge and Se, and the similarity between the coherent neutron scattering lengths for Ge and Se of natural isotopic abundance. Thus, an incident X-ray or neutron cannot distinguish between the Ge and Se atoms in a diffraction experiment, and it follows that $S_X(Q) = S_N(Q) = S_{NN}(Q)$where $S_{NN}(Q)$ denotes the Bhatia–Thornton partial structure factor. It has proved possible, however, to gain site-specific structural information on $GeSe_2$ glass at pressures up to 8.2 GPa using the method of *in situ* high-pressure neutron diffraction with isotope substitution [28], where the diffraction experiments followed the methodology developed in Ref. [36]. The structure of $GeSe_2$ glass was also investigated by conventional neutron diffraction at pressures up to 16.1 GPa [28].

Figure 8(a) and (b) show the measured difference functions $\Delta F_{Ge}(Q)$ and $\Delta F_{Se}(Q)$ for $GeSe_2$ glass, which involve only the Ge or Se atom partial structure factors, respectively. The contrast between these measured difference functions is reproduced by first principles molecular dynamics simulations [28]. At ambient pressure, the network structure of glassy $GeSe_2$ is made from both corner-sharing and edge-sharing Ge-centred tetrahedra (Figure 8(c)), where the latter promote fragile glass-forming behaviour in the associated liquid [37], and the chemical ordering is broken by the appearance of homopolar (like-atom) bonds [38]. This situation is in contrast to oxide glasses such as SiO_2 and GeO_2 where the ambient pressure networks are built solely from corner-sharing Si-centred or Ge-centred

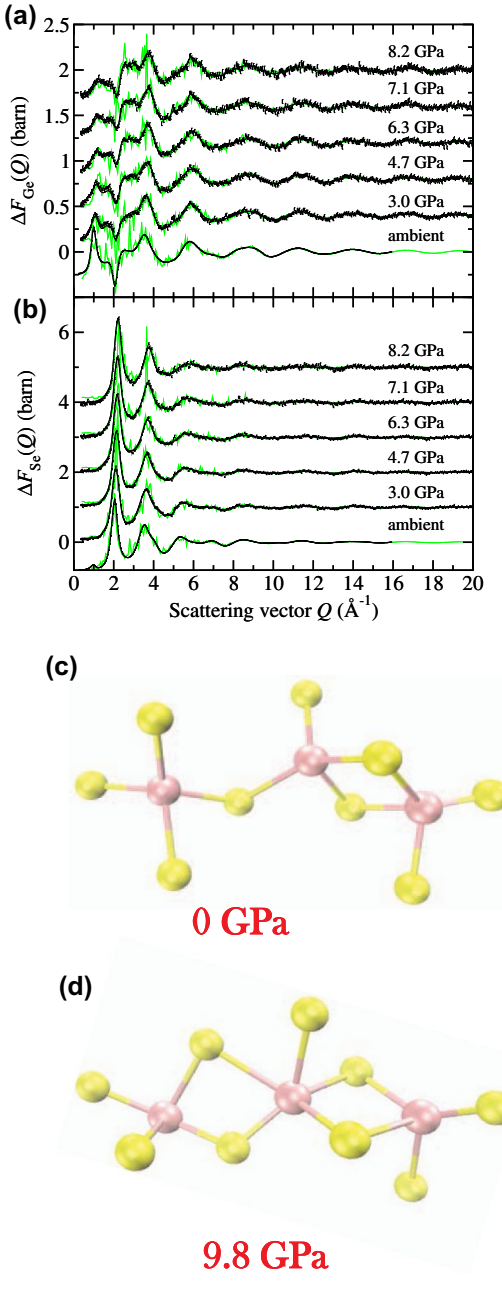

Figure 8. The pressure dependence of the difference functions (a) $\Delta F_{Ge}(Q)$ and (b) $\Delta F_{Se}(Q)$ for $GeSe_2$ glass, as measured using the method of neutron diffraction with isotope substitution (dark (black) curves with vertical error bars) or simulated using first principles molecular dynamics (light [green] curves) [28]. Atomistic configurations taken from the first principles molecular dynamics simulations at (c) ambient pressure, which show both edge and corner-sharing Ge-centred tetrahedra and (d) a pressure of 9.8 GPa, which show typical edge-sharing connections for the polyhedron of a fivefold-coordinated Ge atom. Ge atoms are dark (purple), Se atoms are light (yellow) and bonds are drawn when two atoms are separated by a distance $r \leq r_{cut}$, where the cut-off distance r_{cut} corresponds to the minimum after the first peak in the Ge-Se partial pair-distribution function.

tetrahedra and chemical ordering is maintained. In $GeSe_2$, the edge-sharing tetrahedra persist as important structural motifs as the pressure is increased to ~8.5 GPa, and there is little change in the overall mean coordination number of the chemical species. At higher pressures, the first principles molecular dynamics results find a mediating role for homopolar bonds in the appearance of higher coordinated Ge and Se atoms, where a typical configuration involving a 5-fold coordination Ge atom is shown in Figure 8(d). This stability under load of edge-sharing conformations, and the importance of homopolar bonds in the production of higher coordinated polyhedra, are likely to be generic features in the densification processes for many chalcogenide glasses.

5. Liquids at high pressures and high temperatures

Diffraction experiments on the structure of liquid and glassy materials at *both* high-pressures and high-temperatures present many challenges. In order to achieve pressures in the GPa regime, a small sample needs to be contained within the anvils of a high-pressure press, and it is not therefore possible to use container-less methods in order to achieve high-temperatures. The methodology for high-pressure and high-temperature neutron diffraction experiments on liquid and glassy materials has not been fully developed. It is possible, however, to use XRD with a variety of high-pressure apparatus. For example, a Paris–Edinburgh press can be used in which a resistive heater is contained within the anvils of the press [39] and the background signal is reduced using either stationary collimators in an energy-dispersive set-up [39–42] or an oscillating radial collimator in an angular dispersive set-up [43,44]. Multi-anvil presses have been used extensively to investigate the structure of liquids including metals and semiconductors [45–50]. It is also possible to use a diamond anvil cell and laser heating [51,52]. The Q-range accessible in high-pressure and high-temperature diffraction experiments is usually limited, which leads via Equation (2) to a loss in resolution of features in the $G(r)$ functions that are obtained by Fourier transformation.

5.1. Role of the oxygen packing fraction in the structural transformations of disordered oxide materials

Oxide liquids under geophysical conditions have been the focus of several recent investigations [39–42,45,51,52]. Here, changes in the structure of a melt can affect its transport properties and other physical characteristics such as the compressibility. For example, in silicate melts the rate-of-change of viscosity with pressure changes sign at a pressure for which tetrahedral SiO_4 units are maximally packed [53]. For disordered oxide materials, it has been discovered that the oxygen packing fraction plays an important role in determining when changes in network structures will occur (Figure 9) [54]. For instance, in a wide variety of silicate materials the SiO_4 tetrahedra begin to transform into higher coordinated polyhedra

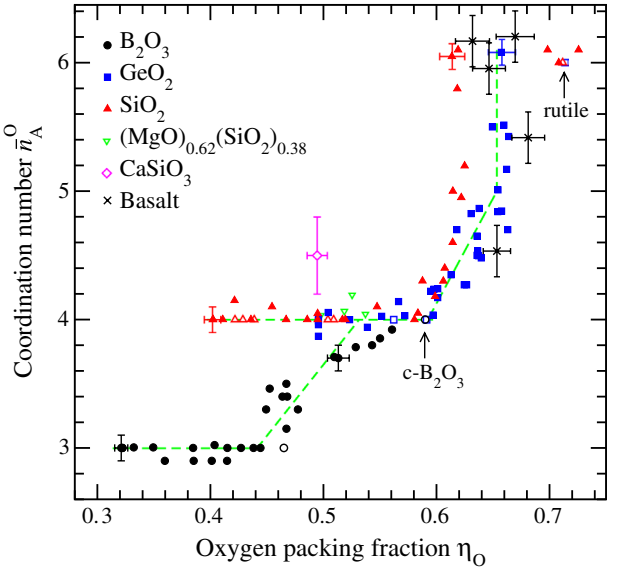

Figure 9. The dependence of the mean A–O coordination number $\bar{n}_A^O$ for network forming motifs (A = B, Si or Ge) on the oxygen packing fraction η_O for glassy B_2O_3, SiO_2, GeO_2 and $(MgO)_{0.62}(SiO_2)_{0.38}$ under cold compression at pressures up to 100 GPa, for liquid $CaSiO_3$ at a temperature of 2130 K and pressure of 6 GPa, and for molten basalt (an aluminosilicate) under deep mantle conditions, i.e. at temperatures in the range 2273–3273 K and pressures up to 60 GPa [25,54].

when the oxygen packing fraction η_O ~0.58, which sits within the range of values found for a random loose packing of hard spheres, and the transformation to SiO_6 octahedra is completed by η_O ~0.64, which corresponds to the value found for a random close packing of hard spheres [54]. The position of the FSDP in disordered oxide materials is sensitive to η_O, and can be used as a marker for when structural transformations are likely to occur [55].

The sensitivity of η_O to structural change most likely originates from an ability of the O^{2-} ion to change its size and shape in response to the coordination environment in which it is confined. For example, in molecular dynamics simulations of the structure of B_2O_3 under compression it is necessary to incorporate both of these features into an ionic interaction model [27], and in the limit when the potential confining an O^2 ion is removed, the isolated ion becomes unstable [56,57].

6. Perspective

We have reviewed recent X-ray and neutron diffraction work on the structure of oxide and chalcogenide liquid and glassy materials under extreme conditions. The results highlight the quality of the experimental information that can now be obtained, which has been made possible by advances in the instrumentation at X-ray synchrotron and neutron sources along with improved measurement

protocols. The work also illustrates how a combination of experiment and simulation can be used in order to understand the structure of disordered materials at both the atomistic and electronic levels. This trend is set to continue, and there is much to look forward to as the experimental methodology is improved to access wider pressure and temperature ranges, thus enabling the structure and properties of materials to be explored under a broader variety of state conditions.

Other quantum-beam diffraction-based techniques can be used to uncover the hidden structure of liquids and glasses, although it is not easy to adopt them for the investigation of these materials under extreme conditions. In the case of electron beams, fluctuation microscopy [58] has recently been used to study continuous random network versus inhomogeneous para-crystalline models for the medium range order in amorphous Si [59], and ångström beam electron diffraction (ABED) has been developed to probe the local atomic configurations and their assemblies in metallic glasses [60,61]. A combination of ABED and high-energy XRD has proved to be a powerful tool for investigating the atomic-scale disproportionation of amorphous silicon monoxide into silicon-like and silicon-dioxide-like regions, and their interface [62]. The development of coherent X-ray beams at next generation synchrotron radiation sources presents an important opportunity for the investigation of disordered materials. Wocher et al. [63] used low-energy coherent X-rays to investigate a colloidal glass of polymethyl methacrylate (PMMA) spheres of radius 117 nm and, by avoiding configurational and temporal averaging, hidden local symmetries were revealed by applying a cross-correlation analysis. The theory of X-ray cross-correlation analysis for investigating the local symmetries in disordered systems is given by Altarelli et al. [64]. Along these lines, it is desirable to promote the development of high-efficiency 2D detectors with sufficient energy discrimination to enable the use of high-energy coherent X-ray scattering methods for exploring the atomic-scale structure of disordered materials.

Acknowledgments

PSS would like to thank James Drewitt and Anita Zeidler for helpful discussions. He would also like to thank Ivy Oxley for her inspiration and encouragement over many years.

Disclosure statement

No potential conflict of interest was reported by the authors.

Funding

This work was supported by JST-PRESTO 'Advanced Materials Informatics through Comprehensive Integration among Theoretical, Experimental, Computational and Data-Centric Sciences'; and 'Materials research by Information Integration' Initiative (MI^2I) project of the Support Programme for Starting Up Innovation Hub from JST.

References

[1] P.A. Egelstaff, Adv. Chem. Phys. 53 (1983) p.1.
[2] C. Massobrio, J. Du, M. Bernasconi and P.S. Salmon (eds.), *Molecular Dynamics Simulations of Disordered Materials: From Network Glasses to Phase-change Memory Alloys, Springer Series in Materials Science 215*, Springer, Cham, 2015.
[3] G.N. Greaves and S. Sen, Adv. Phys. 56 (2007) p.1.
[4] P.S. Salmon and A. Zeidler, Phys. Chem. Chem. Phys. 15 (2013) p.15286.
[5] H.E. Fischer, A.C. Barnes and P.S. Salmon, Rep. Prog. Phys. 69 (2006) p.233.
[6] D.L. Price, *High-temperature Levitated Materials*, Cambridge University Press, Cambridge, 2010.
[7] L.B. Skinner, A.C. Barnes, P.S. Salmon, L. Hennet, H.E. Fischer, C.J. Benmore, S. Kohara, J.K.R. Weber, A. Bytchkov, M.C. Wilding, J.B. Parise, T.O. Farmer, I. Pozdnyakova, S.K. Tumber and K. Ohara, Phys. Rev. B 87 (2013) p.024201.
[8] S. Kohara, J. Akola, L. Patrikeev, M. Ropo, K. Ohara, M. Itou, A. Fujiwara, J. Yahiro, J.T. Okada, T. Ishikawa, A. Mizuno, A. Masuno, Y. Watanabe and T. Usuki, Nat. Commun. 5 (2014) p.5892.
[9] L.B. Skinner, C.J. Benmore, J.K.R. Weber, M.A. Williamson, A. Tamalonis, A. Hebden, T. Wiencek, O.L.G. Alderman, M. Guthrie, L. Leibowitz and J.B. Parise, Science 346 (2014) p.984.
[10] J.W.E. Drewitt, L. Hennet, A. Zeidler, S. Jahn, P.S. Salmon, D.R. Neuville and H.E. Fischer, Phys. Rev. Lett. 109 (2012) p.235501.
[11] J. Akola, S. Kohara, K. Ohara, A. Fujiwara, Y. Watanabe, A. Masuno, T. Usuki, T. Kubo, A. Nakahira, K. Nitta, T. Uruga, J.K.R. Weber and C.J. Benmore, Proc. Natl. Acad. Sci. U.S.A. 110 (2013) p.10129.
[12] S.W. Kim, T. Shimoyama and H. Hosono, Science 333 (2011) p.71.
[13] C. Landron, L. Hennet, T.E. Jenkins, G.N. Greaves, J.P. Coutures and A.K. Soper, Phys. Rev. Lett. 86 (2001) p.4839.
[14] B.T. Poe, P.F. McMillan, B. Coté, D. Massiot and J.-P. Coutures, J. Phys. Chem. 96 (1992) p.8220.
[15] P.S. Salmon, Proc. R. Soc. Lond. A 437 (1992) p.591.
[16] M. Wilson and P.A. Madden, Phys. Rev. Lett. 80 (1998) p.532.
[17] P.S. Salmon, Proc. R. Soc. Lond. A 445 (1994) p.351.
[18] P.S. Salmon, A.C. Barnes, R.A. Martin and G.J. Cuello, Phys. Rev. Lett. 96 (2006) p.235502.
[19] D. Massiot, D. Trumeau, B. Touzo, I. Farnan, J.-C. Rifflet, A. Douy and J.-P. Coutures, J. Phys. Chem. 99 (1995) p.16455.
[20] E. Soignard, C.J. Benmore and J.L. Yarger, Rev. Sci. Instrum. 81 (2010) p.035110.
[21] S. Klotz, *Techniques in High Pressure Neutron Scattering*, CRC Press, Boca Raton, 2013.
[22] J.W.E. Drewitt, P.S. Salmon, A.C. Barnes, S. Klotz, H.E. Fischer and W.A. Crichton, Phys. Rev. B 81 (2010) p.014202.
[23] P.S. Salmon, J.W.E. Drewitt, D.A.J. Whittaker, A. Zeidler, K. Wezka, C.L. Bull, M.G. Tucker, M.C. Wilding, M. Guthrie and D. Marrocchelli, J. Phys. Condens. Matter 24 (2012) p.415102.
[24] T. Hattori, A. Sano-Furukawa, H. Arima, K. Komatsu, A. Yamada, Y. Inamura, T. Nakatani, Y. Seto, T. Nagai, W. Utsumi, T. Iitaka, H. Kagi, Y. Katayama, T. Inoue, T. Otomo, K. Suzuya, T. Kamiyama, M. Arai and T. Yagi, Nucl. Instrum. Methods Phys. Res. A 780 (2015) p.55.
[25] P.S. Salmon and A. Zeidler, J. Phys. Condens. Matter 27 (2015) p.133201.

[26] A. Zeidler, K. Wezka, R.F. Rowlands, D.A.J. Whittaker, P.S. Salmon, A. Polidori, J.W.E. Drewitt, S. Klotz, H.E. Fischer, M.C. Wilding, C.L. Bull, M.G. Tucker and M. Wilson, Phys. Rev. Lett. 113 (2014) p.135501.
[27] A. Zeidler, K. Wezka, D.A.J. Whittaker, P.S. Salmon, A. Baroni, S. Klotz, H.E. Fischer, M.C. Wilding, C.L. Bull, M.G. Tucker, M. Salanne, G. Ferlat and M. Micoulaut, Phys. Rev. B 90 (2014) p.024206.
[28] K. Wezka, A. Bouzid, K.J. Pizzey, P.S. Salmon, A. Zeidler, S. Klotz, H.E. Fischer, C.L. Bull, M.G. Tucker, M. Boero, S. Le Roux, C. Tugène and C. Massobrio, Phys. Rev. B 90 (2014) p.054206.
[29] Y. Inamura, Y. Katayama, W. Utsumi and K.I. Funakoshi, Phys. Rev. Lett. 93 (2004) p.015501.
[30] C.J. Benmore, E. Soignard, S.A. Amin, M. Guthrie, S.D. Shastri, P.L. Lee and J.L. Yarger, Phys. Rev. B 81 (2010) p.054105.
[31] T. Sato and N. Funamori, Phys. Rev. B 82 (2010) p.184102.
[32] P. Tangney and S. Scandolo, J. Chem. Phys. 117 (2002) p.8898.
[33] V.V. Brazhkin, Y. Katayama, K. Trachenko, O.B. Tsiok, A.G. Lyapin, E. Artacho, M. Dove, G. Ferlat, Y. Inamura and H. Saitoh, Phys. Rev. Lett. 101 (2008) p.035702.
[34] S.K. Lee, P.J. Eng, H.-K. Mao, Y. Meng, M. Newville, M.Y. Hu and J. Shu, Nat. Mater. 4 (2005) p.851.
[35] M. Grimsditch, A. Polian and A.C. Wright, Phys. Rev. B 54 (1996) p.152.
[36] K. Wezka, P.S. Salmon, A. Zeidler, D.A.J. Whittaker, J.W.E. Drewitt, S. Klotz, H.E. Fischer and D. Marrocchelli, J. Phys. Condens. Matter 24 (2012) p.502101.
[37] M. Wilson and P.S. Salmon, Phys. Rev. Lett. 103 (2009) p.157801.
[38] I. Petri, P.S. Salmon and H.E. Fischer, Phys. Rev. Lett. 84 (2000) p.2413.
[39] A. Yamada, Y. Wang, T. Inoue, W. Yang, C. Park, T. Yu and G. Shen, Rev. Sci. Instrum. 82 (2011) p.015103.
[40] T. Sakamaki, Y. Wang, C. Park, T. Yu and G. Shen, J. Appl. Phys. 111 (2012) p.112623.
[41] C. Sanloup, J.W.E. Drewitt, C. Crépisson, Y. Kono, C. Park, C. McCammon, L. Hennet, S. Brassamin and A. Bytchkov, Geochim. Cosmochim. Acta 118 (2013) p.118.
[42] T. Sakamaki, Y. Wang, C. Park, T. Yu and G. Shen, Phys. Earth Planet. Int. 228 (2014) p.281.
[43] A. Zeidler, J.W.E. Drewitt, P.S. Salmon, A.C. Barnes, W.A. Crichton, S. Klotz, H.E. Fischer, C.J. Benmore, S. Ramos and A.C. Hannon, J. Phys. Condens. Matter 21 (2009) p.474217.
[44] G. Morard, M. Mezouar, S. Bauchau, M. Álvarez-Murga, J.L. Hodeau and G. Garbarino, Rev. Sci. Instrum. 82 (2011) p.023904.
[45] N. Funamori, S. Yamamoto, T. Yagi and T. Kikegawa, J. Geophys. Res. 109 (2004) p.B03203.
[46] T. Hattori, T. Kinoshita, T. Narushima, K. Tsuji and Y. Katayama, Phys. Rev. B 73 (2006) p.054203.
[47] T. Narushima, T. Hattori, T. Kinoshita, A. Hinzmann and K. Tsuji, Phys. Rev. B 76 (2007) p.104204.
[48] T. Hattori, K. Tsuji, Y. Miyata, T. Sugahara and F. Shimojo, Phys. Rev. B 76 (2007) p.144206.
[49] A. Hinzmann, A. Chiba and K. Tsuji, J. Phys. Condens. Matter 24 (2012) p.115103.
[50] S. Ohmura, A. Chiba, Y. Yanagawa, A. Koura, K. Tsuji and F. Shimojo, J. Phys. Soc. Jpn. 84 (2015) p.094602.
[51] C. Sanloup, J.W.E. Drewitt, Z. Konôpková, P. Dalladay-Simpson, D.M. Morton, N. Rai, W. van Westrenen and W. Morgenroth, Nature 503 (2013) p.104.
[52] J.W.E. Drewitt, S. Jahn, C. Sanloup, C. de Grouchy, G. Garbarino and L. Hennet, J. Phys. Condens. Matter 27 (2015) p.105103.
[53] Y. Wang, T. Sakamaki, L.B. Skinner, Z. Jing, T. Yu, Y. Kono, C. Park, G. Shen, M.L. Rivers and S.R. Sutton Nat. Commun. 5 (2014) p.3241.
[54] A. Zeidler, P.S. Salmon and L.B. Skinner, Proc. Natl. Acad. Sci. U.S.A. 111 (2014) p.10045.

[55] A. Zeidler and P.S. Salmon, Phys. Rev. B 93 (2016) p.214204.
[56] M. Tokonami, Acta Cryst. 19 (1965) p.486.
[57] P. Jemmer, P.W. Fowler, M. Wilson and P.A. Madden, J. Phys. Chem. A 102 (1998) p.8377.
[58] M.M.J. Treacy, J.M. Gibson, L. Fan, D.J. Paterson and I. McNulty, Rep. Prog. Phys. 68 (2005) p.2899.
[59] M.M.J. Treacy and K.B. Borisenko, Science 335 (2012) p.950.
[60] A. Hirata, P. Guan, T. Fujita, Y. Hirotsu, A. Inoue, A.R. Yavari, T. Sakurai and M.W. Chen, Nat. Mater. 10 (2011) p.28.
[61] A. Hirata, L.J. Kang, T. Fujita, B. Klumov, K. Matsue, M. Kotani, A.R. Yavari and M.W. Chen, Science 341 (2013) p.376.
[62] A. Hirata, S. Kohara, T. Asada, M. Arao, C. Yogi, H. Imai, Y. Tan, T. Fujita and M.W. Chen, Nat. Commun. 7 (2016) p.11591.
[63] P. Wochner, C. Gutt, T. Autenrieth, T. Demmer, V. Bugaev, A.D. Ortiz, A. Duri, F. Zontone, G. Grübel and H. Dosch, Proc. Natl. Acad. Sci. U.S.A. 106 (2009) p.11511.
[64] M. Altarelli, R.P. Kurta and I.A. Vartanyants, Phys. Rev. B 82 (2010) p.104207.